Japanese Journal of
Applied Physics

REGULAR PAPER • **OPEN ACCESS**

Thin and locally dislocation-free SiGe virtual substrate fabrication by lateral selective growth

To cite this article: Yuji Yamamoto *et al* 2024 *Jpn. J. Appl. Phys.* **63** 02SP53

OPEN ACCESS

Japanese Journal of Applied Physics **63**, 02SP53 (2024) **REGULAR PAPER**

https://doi.org/**10.35848/1347-4065/ad189d**

Thin and locally dislocation-free SiGe virtual substrate fabrication by lateral selective growth

Yuji Yamamoto[1*], Wei-Chen Wen[1], Markus Andreas Schubert[1], Agnieszka Anna Corley-Wiciak[1,2], Sho Sugawa[3], Yuta Ito[3], Ryo Yokogawa[3], Han Han[4], Roger Loo[4,5], Atsushi Ogura[3], and Bernd Tillack[1,6]

[1]*IHP - Leibniz-Institut für innovative Mikroelektronik, Im Technologiepark 25, D-15236 Frankfurt (Oder), Germany*
[2]*RWTH Aachen University, D-52056, Aachen, Germany*
[3]*School of Science and Technology, Meiji University, 1-1-1 Higashimita, Tama-ku, Kawasaki, Kanagawa 214-8571, Japan*
[4]*imec, vzw, Kapeldreef 75, B-3001 Leuven, Belgium*
[5]*Ghent University, Department of Solid-State Sciences, Krijgslaan 281, building S1, B-9000 Ghent, Belgium*
[6]*Technische Universität Berlin, HFT4, Einsteinufer 25, D-10587 Berlin, Germany*

[*]E-mail: yamamoto@ihp-microelectronics.com

Received October 13, 2023; revised December 2, 2023; accepted December 24, 2023; published online January 17, 2024

Locally dislocation-free SiGe-on-insulator (SGOI) is fabricated by CVD. Lateral selective SiGe growth of ~30%, ~45% and ~55% of Ge content is performed around ~1 μm square Si(001) pillar located under the center of a 6.3 μm square SiO_2 on Si-on-insulator substrate which is formed by H_2-HCl vapor-phase etching. In the deposited SiGe layer, tensile strain is observed by top-view. The degree of strain is slightly increased at the corner of the SiGe. The tensile strain is caused by the partial compressive strain of SiGe in lateral direction and thermal expansion difference between Si and SiGe. Slightly higher Ge incorporation is observed in higher tensile strain region. At the peaks formed between the facets of growth front, Ge incorporation is reduced. These phenomena are pronounced for SiGe with higher Ge contents. Locally dislocation-free SGOI, which is beneficial for emerging device integration, is formed along ⟨010⟩ from the Si pillar by lateral aspect-ratio-trapping.

1. Introduction

Virtual substrates (VS) of group IV materials such as SiGe and Ge are essential for fabricating high-performance and emerging devices.[1–5] However, because the SiGe VS is fabricated by heteroepitaxy on a Si substrate, strain is formed at the interface. Therefore, surface roughening and crystalline defect formation, which are caused by the strain fluctuation, cannot be avoided. In order to apply the SiGe VS for high-performance devices, the VS with high quality and uniform strain distribution is required. Various techniques to grow high crystallinity planer VS are reported, e.g. conventional graded buffers[6–10] and reverse graded buffers.[11–14] However, there are still several remaining problems with these methods as they require several μm thick buffer layers to reduce threading dislocation (TD) density. The distribution of TD networks in the SiGe layer causes uncontrolled random positions of the TDs. Additionally, strain fluctuation due to misfit dislocations (MDs) and TDs causes crosshatch pattern formation resulting in high surface roughness and tilt-lattice plane at the SiGe VS surface.[15,16] The surface roughness can be planarized by chemical mechanical polishing (CMP), however, the random distribution of the TDs and the fluctuation of the SiGe lattice plane tilt cannot be solved by the CMP process. Additionally, the high SiGe VS thickness causes difficulties for local interconnections between devices on the SiGe VS and those on Si. Therefore, the process development of thin SiGe VS with controlled distribution of defects is of interest.

Another approach to high crystal quality heteroepitaxial VS growth is aspect-ratio-trapping (ART).[17–21] By depositing heteroepitaxial material in a high aspect-ratio window, whose height/width ratio is typically higher than ~1.4, the TDs can be trapped at sidewalls because the TDs are grown on (111) plane. After trapping the TDs, the upper part of the selectively grown SiGe and Ge layers become theoretically dislocation-free. However, if the window is line structure along [110] direction, the ART works for TDs for all directions, but planer defects such as stacking faults (SFs) cannot be trapped along [110] direction, because the SF is existing on (111) plane and parallel to [110] direction.[19]

Another unique approach is nano-hetero-epitaxy (NHE).[22–25] By depositing SiGe or Ge selectively on Si nano-pillars, strain is accumulated not only in the deposited SiGe and Ge part but also in the Si pillar by elastic deformation through expanding in lateral direction. By transferring the strain energy partially to the Si side, relaxed Ge growth without misfit dislocation formation can be enabled resulting infinite critical thickness.[24,25] The problem of both the ART and the NHE, is that the dislocation-free area is limited to a very small area only.

In our previous works, lateral selective Ge growth was performed in a cavity formed by selective vapor-phase etching (VPE) of Si from the side of mesa-patterned SiO_2/Si-on-insulator (SOI) wafer.[26] By the lateral selective growth of Ge, locally dislocation-free, thin and smooth Ge-on-insulator is fabricated by the horizontal ART mechanism. Using the lateral selective growth approach, the feasibility of SiGe-on-insulator (SGOI) fabrication is also reported.[27] By the lateral selective growth approach, several-μm square of dislocation-free area of Ge and SiGe are realized.[26–28] The location of the dislocation-free area is controlled, potentially it is possible to fabricate devices on the dislocation-free area by circuit design.

In ssdm-2023, we presented the lateral selective SiGe growth with different Ge contents and discussed the dependency of the Ge concentration on the strain and Ge distributions.[28] In this paper, in addition to the content in ssdm-2023 extended abstract,[28] distributions of Ge concentrations along [110] and defects are confirmed by energy

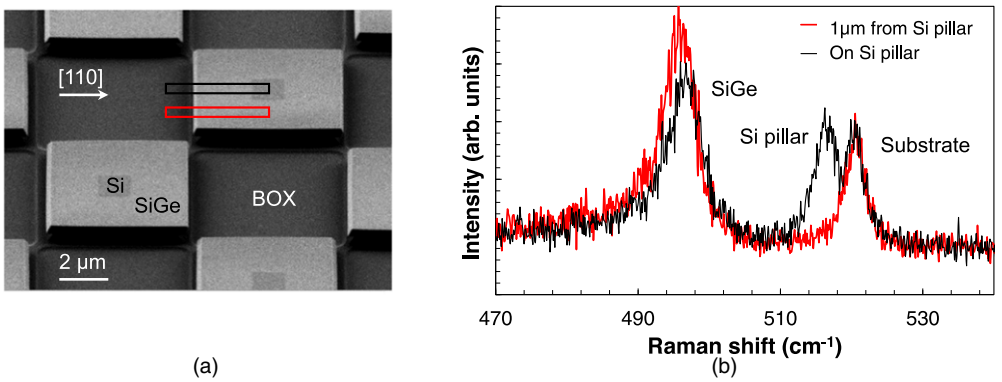

Fig. 1. (a) Angle-view SEM image of laterally grown selective SiGe around a Si pillar and (b) μ-Raman spectra of Si–Si vibration mode measured at the red and black rectangle regions in (a). Green laser of 523 nm wavelength is used for the μ-Raman measurement. The top SiO_2 is removed by HF. The Ge concentration measured by EDX is ~45%.

dispersive X-ray spectroscopy (EDX) and electron channeling contrast imaging (ECCI), respectively.

2. Experimental methods

Lateral selective growth of SiGe in the cavity is carried out using a reduced-pressure (RP) chemical vapor deposition (CVD) system. SOI wafers with (001) crystal orientation are used. For sample preparation, an epitaxial Si layer is deposited on the SOI wafer to adjust to 420 nm thick SOI. Afterward, the SOI is thermally oxidized to form 300 nm thick SiO_2 cap and 300 nm Si on buried oxide (BOX). Then, 6.3 μm square checkerboard SiO_2/Si mesa structures with ⟨110⟩ oriented sidewalls are fabricated by photolithography and dry etching of the SiO_2 cap and SOI. In order to ensure prevention of SiGe nucleation especially on the sidewalls of the mesas, thermal oxidation of ~10 nm is additionally performed from the sidewalls of the mesas and the HF dip is performed to re-open the Si sidewalls to clean potential nucleation sites due to residual organic contaminations by the dry etching process. After the patterning, the 300 nm thick Si sidewalls are opened and all the rest of the wafer surface is covered by SiO_2.

After following a standard RCA clean and an HF dip, the wafer is loaded into the RPCVD reactor and prebaked at 850 °C in RP H_2 to remove residual oxide on the Si sidewalls. Afterward, a cavity held by a ~1 μm square Si pillar at the center of the mesa is fabricated by H_2-HCl VPE of Si at 850 °C at atmospheric pressure. Then, SiGe layers with a Ge content of ~30%, ~45%, and ~55% (measured by EDX spectroscopy) are selectively deposited by using H_2-SiH_2Cl_2-GeH_4-HCl gas system in the cavity around the Si pillar at 750 °C, 700 °C and 675 °C, respectively. In order to exclude impact of a microloading effect on the SiGe growth, the growth rate of the selective SiGe growth is set at ~4 nm min^{-1}. for ignorable depletion of reactant gases. Finally, the top SiO_2 is removed by HF.

Scanning electron microscope (SEM) is used for inspecting the selectivity and morphology of the Si pillar and the laterally grown SiGe. Scanning transmission electron microscopy (STEM) is used for defect analysis. EDX with below 1 nm beam size is used for evaluating Ge contents and distributions. Micro-Raman (μ-Raman) spectroscopy using 500 nm spot size green laser of 532 nm wavelength is applied for analyzing distribution of strain and Ge concentration. For the strain and the Ge concentration mapping, the spectra are scanned by 200 nm step. ECCI is also performed for defect inspection.

3. Results and discussion

3.1. Distribution of strain in the laterally grown SiGe

Figure 1(a) shows an angle view SEM image of a sample of laterally grown SiGe containing ~45% Ge on the SiO_2 surfaces. No polycrystalline nucleation is observed indicating the SiGe growth is highly selective, and the sharp and straight edge of the sidewall shape indicates a good crystal quality of the SiGe layer. A smooth SiGe surface is obtained, because the roughness is determined by the interface between SiO_2 and Si.[26,27] The μ-Raman spectrum of Si–Si vibration mode measured in the black rectangle in Fig. 1(a) shows peaks at 496.6 cm^{-1}, 516.0 cm^{-1}, and 520.5 cm^{-1}, which correspond to the SiGe, Si pillar and Si substrate, respectively [Fig. 1(b)]. The peak position of Si pillar is ~4.5 cm^{-1} shifted to lower wavenumber from the Si substrate peak. This is caused by tensile strain of ~0.5% in the Si pillar. A possible reason for the formation of tensile strain in the Si pillar is the HCl VPE and/or the following lateral selective growth of SiGe, because at the initial stage, the SiGe growth is pseudomorphically grown against the Si sidewalls. The SOI is compressively strained during the HCl VPE process at 850 °C, because Si has a higher thermal expansion coefficient compared to SiO_2.[29] During the HCl VPE, the interface area of the Si pillar and SiO_2 becomes smaller since the SOI is etched from all sides of the mesa structures. Due to the reduced area, the mechanical robustness of the interface becomes weaker. The weakened robustness may cause slipping of the interface to compensate for the compressive strain of the Si pillar at 850 °C. After following the SiGe growth, the wafer is cooled down to RT. Si pillar seems to be pinned with the BOX and the SiO_2 cap during the cooling because of lower thermal energy, resulting in tensile strain formation. In the μ-Raman spectrum measured at ~1 μm away from the Si pillar toward [1–10] direction [Shown as a red rectangle in Fig. 1(a)], the Si–Si peak at 516.0 cm^{-1} assigned to the Si pillar has disappeared. This means that the Si pillar is not sensed by the laser spot of the μ-Raman measurement. The Si–Si peak from the Si substrate is unchanged, but the peak from the SiGe becomes slightly wider and the position is shifted to ~495.8 cm^{-1} and becomes slightly wider. This result indicates the presence of

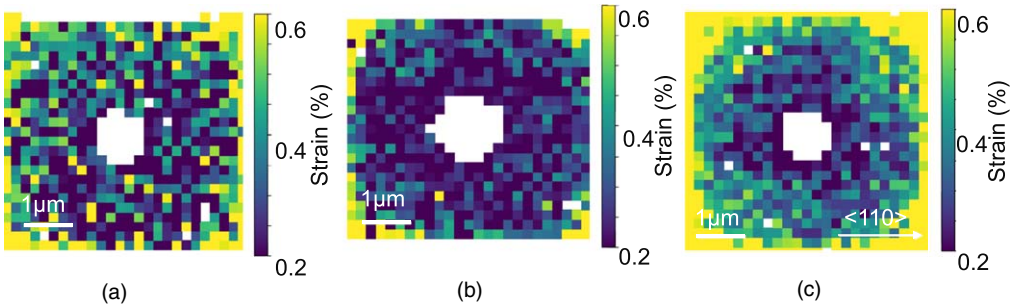

Fig. 2. Mapping of strain distributions of laterally grown SiGe measured by μ-Raman spectroscopy. Green laser of 523 nm wavelength is used for the measurement. Estimated Ge concentrations by EDX are (a) ∼30%, (b) ∼45% and (c) ∼55%.

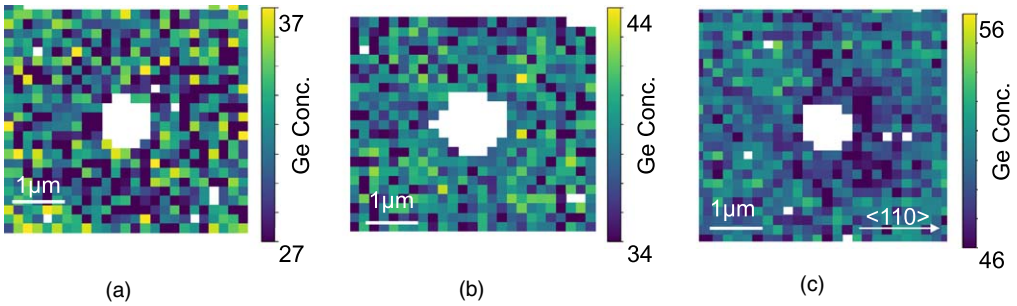

Fig. 3. Mapping Ge concentration distributions of laterally grown SiGe measured by μ-Raman spectroscopy. Green laser of 523 nm wavelength is used for the measurement. Estimated Ge concentrations by EDX are (a) ∼30%, (b) ∼45% and (c) ∼55%.

non-uniform tensile strain and/or Ge composition in the SiGe. Because SiGe material properties along [1–10] and [−1–10] directions from the Si pillar are the same (only 90° rotated), the position of the peak component from SiGe layer in [−110] direction is the same as the black peak in Fig. 1(b). That means, that the slight red-shift of the peak from the SiGe layer is from the SiGe in diagonal direction from the Si pillar.

In order to discuss the detail of the strain distribution within the SiGe layers, strain mappings of SiGe with ∼30%, ∼45%, and ∼55% measured by μ-Raman spectroscopy are shown in Figs. 2(a)–2(c), respectively. Biaxial strain and composition of SiGe were evaluated using the peak energy Ge–Ge (∼290 cm^{-1}), Si–Ge (∼405 cm^{-1}) and Si–Si (∼500 cm^{-1}) modes. Using the parameters and the method reported in,[30] the composition and biaxial strain can be calculated at each point of the map by using following formulas;

$$\omega^{\mathrm{Si-Si}}(x, \varepsilon) = 520.7 - 66.9x - 730\varepsilon \quad (1)$$

$$\omega^{\mathrm{Si-Ge}}(x, \varepsilon) = 400.1 + 24.5x - 4.5x^2 - 33.5x^3 - 730\varepsilon \quad (2)$$

$$\omega^{\mathrm{Ge-Ge}}(x, \varepsilon) = 280.3 + 19.4x - 450\varepsilon \quad (3)$$

where $\omega^{\mathrm{Si-Si}}$, $\omega^{\mathrm{Si-Ge}}$, and $\omega^{\mathrm{Si-Ge}}$ are wavenumbers of Si–Si, Si–Ge, and Ge–Ge vibration modes, respectively, x is Ge composition and ε is biaxial strain.

For all SiGe samples with ∼30%, ∼45% and ∼55% Ge contents, tensile strain is observed in the laterally grown SiGe layer, and a higher degree of strain is observed near the growth front of the SiGe layer. A pronounced increase of strain at the edge is observed for the sample with higher Ge content. For the SiGe layer, almost no explicit growth direction dependency of strain deviation is noticed for the ∼30% SiGe [Fig. 2(a)]. However, in the case of the ∼45% and ∼55% SiGe samples, slightly higher tensile strain can be recognized along ⟨010⟩ directions from the Si pillar compared to ⟨110⟩ directions. These results are supported by Fig. 1(b). The tensile strain in SiGe and its distribution can be explained as follows;

1. During the first stage of the SiGe growth, the laterally selectively grown SiGe is pseudomorphically grown and its relaxation starts gradually. The degree of relaxation cannot reach 100%. i.e. the laterally grown SiGe is partially compressively strained in perpendicular to the growth front directions. The remaining compressive strain in the lateral direction is observed as a tensile strain from top-view.
2. The thermal expansion coefficient of SiGe is higher compared to Si. Therefore, additional tensile strain is formed in the SiGe during cooling down from growth temperature to RT. The tensile strain due to thermal expansion is perpendicular to the SiGe growth direction, therefore the degree of tensile strain from top-view should be slightly compensated.
3. Slightly higher tensile strain is observed along ⟨010⟩ directions from the Si pillar compared to ⟨110⟩ directions because the SiGe located in the diagonal direction is pulled by biaxial directions.

3.2. Distribution of Ge composition in the laterally grown SiGe

Figures 3(a)–3(c) shows the Ge concentration mappings of the laterally grown SiGe with ∼30%, ∼45% and ∼55% Ge shown in Figs. 2(a)–2(c). In the sample with ∼30% Ge [Fig. 3(a)], no clear distribution of Ge content is observed. However, in the case of ∼45% and ∼55% SiGe [Figs. 3(b), 3(c)], slightly greenish color is observed. in diagonal regions. That means Ge content along the ⟨010⟩ directions is a slightly

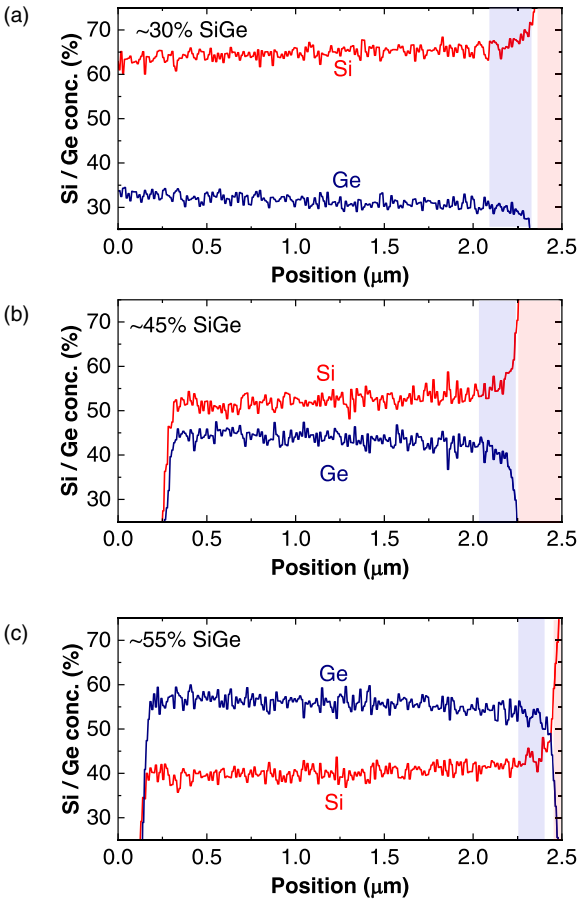

Fig. 4. Cross sectional Ge concentration profiles of laterally grown SiGe with (a) ~30%, (b) ~45% and (c) ~55% Ge content measured by EDX. TEM lamellas are cut out along [110] direction from the Si pillar. The Si pillar part is marked by the red shadow. The rapidly increased Ge content part in the SiGe near the SiGe/Si interface is marked by the blue shadow.

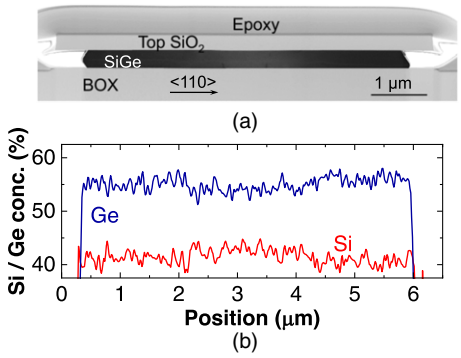

Fig. 5. (a) Cross section bright field STEM image of ~1 μm toward ⟨110⟩ direction from Si pillar. Lamella of the specimen is cut out ~1 μm away from Si pillar toward [−110] direction. (b) Line profiles of Si and SiGe of the laterally grown SiGe measured by EDX. Estimated Ge concentration is ~55%.

higher compared to the ⟨110⟩ directions. In the diagonal directions of these samples, slightly higher tensile strain is observed as shown in Figs. 2(b), 2(c). Apparently, a higher tensile strain enhances the Ge incorporation during the SiGe growth. A similar result is also reported in.[31] However, further investigation is required to clarify the mechanism behind it.

Next, the Ge incorporation during the SiGe growth is discussed. Figures 4(a)–4(c) show the Ge concentration profiles of ~30%, ~45% and ~55% SiGe along [110] direction from the Si pillar [same position as black square in Fig. 1(a)] measured by EDX, respectively. For all samples, the SiGe growth starts within relatively lower Ge content and rapidly rises (marked with blue color in each figure). The thicknesses for the rapidly increased part are ~500 nm, ~400 nm and ~300 nm for the samples containing ~30%, ~45% and ~55% Ge, respectively. After that the Ge concentration in the SiGe layer increases very slowly during the following layer growth. A possible reason for the increase may be plastic relaxation of the SiGe.[32] During the lateral SiGe growth, faster plastic relaxation of SiGe occurs at first and then further relaxation proceeds gradually and moderately. In the case of SiGe layers with a higher Ge content, the plastic relaxation proceeds faster compared to the SiGe with a lower Ge content. The thickness of the rapidly increased Ge concentration part reduces with increasing Ge content. This could be caused by the fast relaxation during the initial stage.

An increase of the Ge concentration along ⟨010⟩ direction starting from the Si pillar compared to that along the ⟨110⟩ direction has been confirmed by cross-section STEM as shown in Fig. 5(a) for the SiGe sample with ~55% Ge content. The TEM lamella is cut out from ~1 μm away from the Si pillar toward [−110] direction. Profiles of the Ge and Si presented in Fig. 5(a) are shown in Fig. 5(b). The Ge concentration at the center area is ~54%, while the Ge concentration in the right and left area is ~55%. Accordingly, the Si concentration in the right and left area is slightly decreased. For both ~54% and ~55% regions, relative uniform Ge composition is observed within each region. A slightly higher Ge concentration in the diagonal directions from the Si pillar is confirmed. This EDX result supports the higher Ge concentration along the diagonal area shown in Fig. 3(c). As shown in Fig. 2(c), tensile strain in the diagonal area is slightly higher compared to ⟨110⟩ directions from Si pillar. This result also supports the slightly higher Ge concentration corelated with the higher tensile strain in the ⟨010⟩ directions compared to the ⟨110⟩ directions.

Figures 6(a), 6(b) show cross-section STEM images of SiGe containing ~30% and ~55% Ge. Additionally, vertical Ge concentration profiles [marked as red rectangles in Figs. 6(a), 6(b)] are shown in Figs. 6(c), 6(d). A bright line contrast is observed at the center of the SiGe layer [Fig. 6(a)]. The bright line reflects the presence of a reduced Ge concentration plane [Fig. 6(c)]. The bright line extends to a peak of growth front surface. This phenomenon is also observed for the ~45% SiGe (not shown). Apparently, the Ge incorporation is influenced by facet orientation.[33] On the other hand, the line of the reduced Ge concentration plane is not clearly observed for SiGe with ~30% Ge content [Figs. 6(b), 6(d)]. It seems that the influence of the facet orientation on Ge incorporation is less sensitive for lower Ge concentration.

Figure 7 displays, plan-view Ge concentration mapping of SiGe with ~55% Ge content measured by EDX. In order to visualize the small change in the Ge content, the color contrast is highly increased in this image. A slightly darker color is visible in ⟨110⟩ directions from the Si pillar

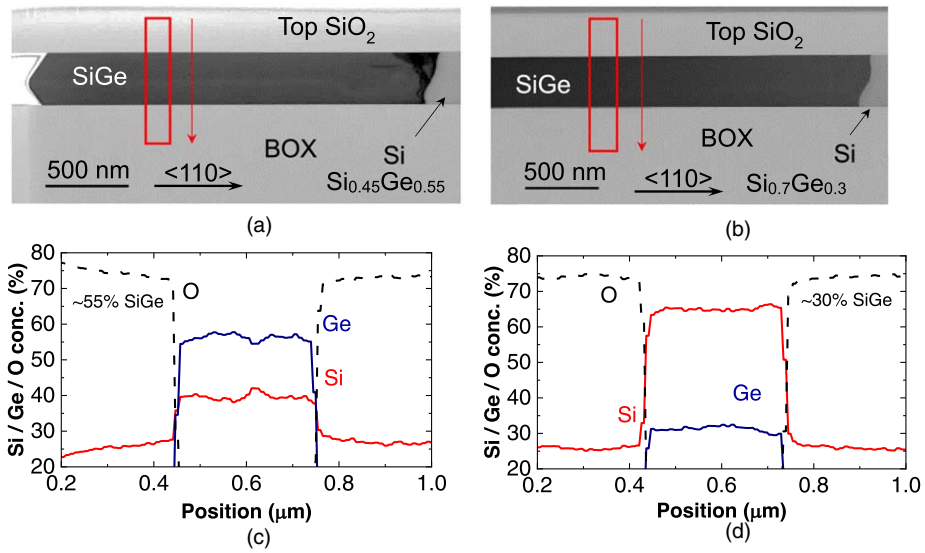

Fig. 6. Cross sectional bright field STEM images of SiGe with (a) ∼55% Ge content and (b) ∼30% Ge content. (c) and (d) shows EDX line profiles of the SiGe with ∼55% and ∼30% Ge content which are marked with red rectangles in (a) and (b), respectively.

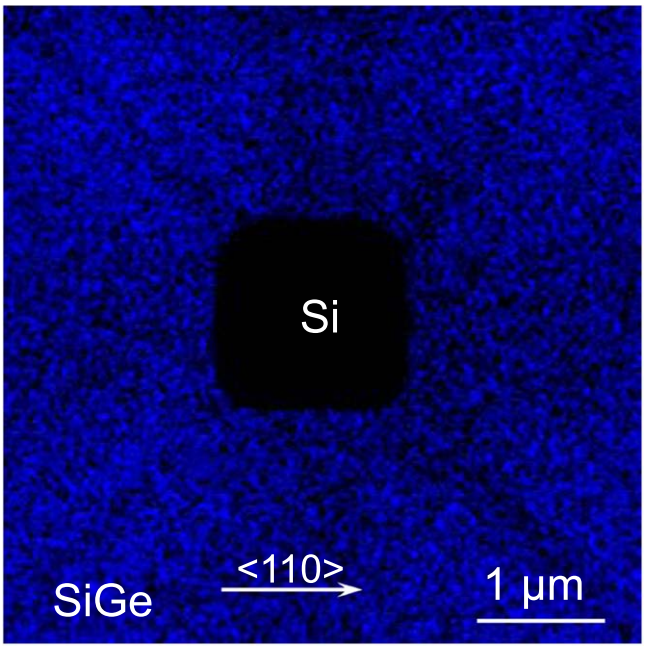

Fig. 7. EDX mapping image of Ge concentration of laterally grown SiGe around the Si pillar with ∼55% Ge content. In order to visualize small difference in Ge composition, color contrast is highly enhanced.

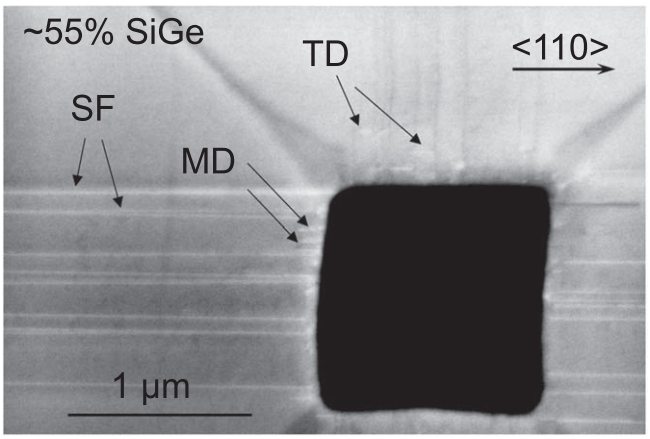

Fig. 8. ECCI of laterally grown SiGe around the Si pillar containing ∼55% Ge. SFs, MDs and TDs are marked with arrows.

compared to the diagonal area, indicating a slightly lower Ge concentration. This is in agreement with the results shown in Figs. 3(c) and 5. Additionally, along ⟨010⟩ direction, relatively sharp dark lines are observed. The diagonal dark lines indicate reduced Ge concentration planes and they start from the corners of the Si pillar to the corner of the laterally grown SiGe. The reduced Ge concentration plane is also related to the peak between the facets of the SiGe growth front, which is according to mechanism as shown in Figs. 6(a), 6(c).

3.3. Distribution of defects in the laterally grown SiGe

Finally, the distribution of defects in the SiGe is discussed. Figure 8 shows the plan-view ECCI of the SiGe containing ∼55% Ge is shown. In the ECCI, SFs are observed along ⟨110⟩ orientations. MDs and TDs are observed at the SiGe/Si interfaces and the SiGe near the interface, respectively. Because the SFs are on the (111) plane, the direction of the SFs is limited to the ⟨110⟩ directions only. Along ⟨010⟩ directions, the dark contrast lines, which are due to the reduced Ge concentration planes (as shown in Fig. 7), are started at the corner of the Si pillar. The width of the reduced Ge concentration plane is wide and becomes narrower in the direction away from the Si pillar. The contrast lines trace the corner of the laterally grown selective SiGe. The change of the reduced Ge concentration plane area is related to facet formation at the corner in the initial stage of the SiGe growth.

Figures 9(a), 9(b) shows plan-view STEM images of the laterally grown SiGe around the Si pillar containing ∼55% and ∼30% Ge, respectively. In Fig. 9(a), long SFs along ⟨110⟩ directions from the Si pillar are observed. MDs exists at the interface between the Si pillar and the SiGe, and TDs are observed in the SiGe near the interface, indicating ART is working in the lateral direction. This result supports the ECCI-observations shown in Fig. 8. In the case of sample with ∼30% SiGe [Fig. 9(b)], a smaller number of SFs, MDs and TDs is observed. The lower densities of SF, MD and TDs are caused by the lower lattice mismatch between Si pillar and SiGe. For both samples line contrast along ⟨010⟩

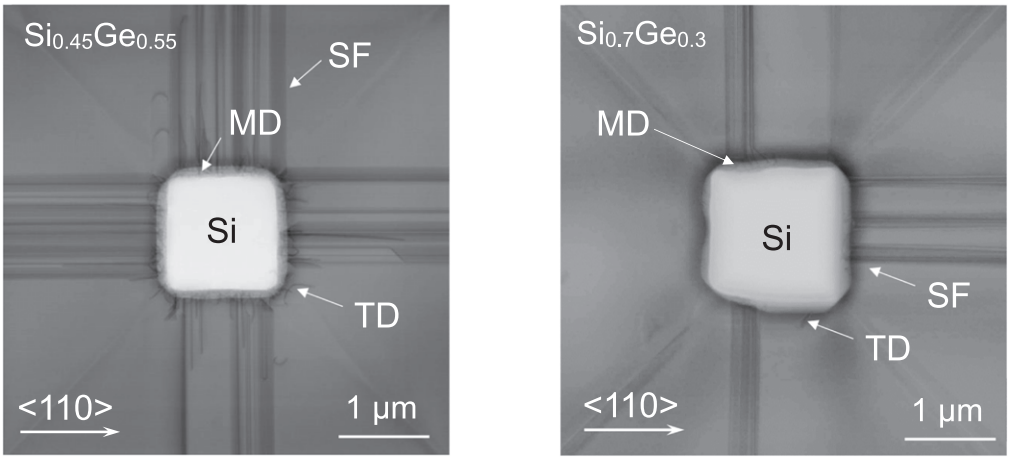

Fig. 9. Plan-view bright field STEM images of laterally grown SiGe containing (a) ∼55% Ge and (b) ∼30% Ge. SFs, MDs and TDs are marked with arrows.

directions due to the Ge concentration drop are also visible. As shown in Fig. 9(a) no dislocations are existing in the SiGe along ⟨010⟩ from the Si pillar [both right and left side in Fig. 9(a)]. Furthermore, by tilting measurement angle of the TEM lamella, the contrast of the diagonal line is not changed (not shown). Therefore, the diagonal contrast is not related to fluctuation of strain and defects. The wide dislocation-free SiGe area along ⟨010⟩ directions from the Si pillar is confirmed by both plan-view ECCI and STEM images.

4. Conclusions

Locally dislocation-free SGOI is fabricated by RPCVD by using H_2-SiH_2Cl_2-GeH_4-HCl gas mixture. Lateral selective SiGe growth containing ∼30, ∼45 and ∼55% Ge around ∼1 μm square Si(001) pillar located under the center of a 6.3 μm square SiO_2 on SOI substrate has been demonstrated. In the laterally grown SiGe, tensile strain is observed. The tensile strain is caused by the difference in thermal expansion between Si and SiGe and by the partial compressive strain of SiGe in lateral direction. The degree of the strain is slightly higher at the corner of the SiGe because the diagonal area is pulled by both [1–10] and [−1–10] directions. The Ge incorporation is increased by the tensile strain. At the peak between the facets at the growth front of SiGe, a reduced Ge incorporation is observed. These phenomena are more pronounced for the SiGe layers with a higher Ge content. The wide dislocation-free area is formed along ⟨010⟩ from the Si pillar by lateral ART. Strain management and facet formation control are key for realizing uniform locally dislocation-free SGOI by lateral selective growth.

Acknowledgments

The authors thank the IHP cleanroom staff for technical support.

ORCID iDs

Yuji Yamamoto https://orcid.org/0000-0003-0928-4356
Wei-Chen Wen https://orcid.org/0000-0001-6804-9562
Agnieszka Anna Corley-Wiciak https://orcid.org/0000-0003-0974-1190
Ryo Yokogawa https://orcid.org/0000-0003-1762-4664
Han Han https://orcid.org/0000-0003-2169-8332
Roger Loo https://orcid.org/0000-0003-3513-6058
Atsushi Ogura https://orcid.org/0000-0003-2008-7695

1) M. De Michielis, E. Ferraro, E. Prati, L. Hutin, B. Bertrand, E. Charbon, D. J. Ibberson, and M. Fernando Gonzalez-Zalba, J. Phys. D: Appl. Phys. **56**, 363001 (2023).
2) W. M. Chen, P. J. McNally, G. D. M. Dilliway, J. Bonar, T. Tuomi, and A. F. W. Willoughby, J. Mate. Sci.: Mater. Electron. **14**, 455 (2003).
3) R. Loo et al., ECS J. Solid State Sci. Technol **6**, 14 (2017).
4) D. Marris-Morini, P. Chaisakul, M.-S. Rouifed, J. Frigerio, D. Chrastina, G. Isella, S. Edmond, X. Le Roux, J.-R. Coudevylle, and L. Vivien, Nanophotonics **2**, 279 (2013).
5) E. A. Fitzgerald, Y. H. Xie, M. L. Green, D. Brasen, A. R. Kortan, J. Michel, Y.-J. Mii, and B. E. Weir, Appl. Phys. Lett. **59**, 811 (1991).
6) E. T. Simola et al., Phys. Rev. Appl. **19**, 014011 (2023).
7) D. Chrastina, G. Isella, M. Bollani, B. Rössner, E. Müller, T. Hackbarth, E. Wintersberger, Z. Zhong, J. Stangl, and H. von Känel Asdfasdf, J. Cryst. Growth **281**, 281 (2005).
8) Y. Bogumilowicz, J. M. Hartmann, F. Laugier, G. Rolland, T. Billon, N. Cherkashin, and A. Claverie, J. Cryst. Growth **283**, 346 (2005).
9) N. Franco, N. P. Barradas, E. Alves, A. M. Vallêra, R. J. H. Morris, O. A. Mironov, and E. H. C. Parker, Mater. Sci. Eng: B **124–125**, 123 (2005).
10) S. Cecchi, E. Gatti, D. Chrastina, J. Frigerio, E. Muller Gubler, D. J. Paul, M. Guzzi, and G. Isella, J. Appl. Phys. **115**, 093502 (2014).
11) V. A. Shah, A. Dobbie, M. Myronov, D. J. F. Fulgoni, L. J. Nash, and D. R. Leadley, Appl. Phys. Lett. **93**, 192103 (2008).
12) V. A. Shah, A. Dobbie, M. Myronov, and D. R. Leadley, J. Appl. Phys. **107**, 064304 (2010).
13) O. Skibitzki et al., Phys. Rev. Mater. **4**, 103403 (2020).
14) V. Sivadasan, S. Rhead, D. Leadley, and M. Myronov, Semicond. Sci. Technol. **33**, 024002 (2018).
15) H. Seng, T. Osipowicz, J. Zhang, and E. S. Tok, Appl. Phys. A **81**, 1163 (2005).
16) M. H. Zoellner et al., ACS Appl. Mater. Interfaces **7**, 9031 (2015).
17) J. G. Fiorenza, J.-S. Park, J. Hydrick, J. Li, J. Li, M. Curtin, M. Carroll, and A. Lochtefeld, ECS Trans. **33**, 963 (2010).
18) J.-S. Park, J. Bai, M. Curtin, B. Adekore, M. Carroll, and A. Lochtefeld, Appl. Phys. Lett. **90**, 052113 (2007).
19) J. Bai, J.-S. Park, Z. Cheng, M. Curtin, B. Adekore, M. Carroll, A. Lochtefeld, and M. Dudley, Appl. Phys. Lett. **90**, 101902 (2007).
20) T. Orzali, A. Vert, B. O'Brien, J. L. Herman, S. Vivekanand, R. J. W. Hill, Z. Karim, and S. S. Papa Rao, J. Appl. Phys. **118**, 105307 (2015).
21) J. Z. Lia, J. Baia, J. M. Hydricka, J. G. Fiorenzaa, C. Majora, M. Carrolla, Z. Shellenbargerb, and A. Lochtefelda, ECS Trans. **18**, 887 (2009).
22) D. Zubia, S. H. Zaidi, S. D. Hersee, and S. R. J. Brueck, J. Vac. Sci. Technol. B **18**, 3514 (2000).
23) P. Zaumseil, Y. Yamamoto, M. A. Shubeert, and T. Schroeder, Thin Solid Films **557**, 50 (2014).
24) Y. Yamamoto, P. Zaumseil, M. A. Schubert, G. Capellini, M. Salvalaglio, F. Montalenti, T. Schroeder, and B. Tillack, Mater. Sci. Semicond. Proc. **70**, 30 (2017).

25) P. Zaumseil, Y. Yamamoto, M. A. Schubert, G. Capellini, O. Skibitzki, M. H. Zoellner, and T. Schroeder, Nanotechnology **26**, 355707 (2015).
26) Y. Yamamoto, M. A. Schubert, C. Reich, and B. Tillack, ECS J. Solid State Sci. Technol. **3**, 353 (2014).
27) K. Anand, M. A. Schubert, A. A. Corley-Wiciak, D. Spirito, C. Corley-Wiciak, W. M. Klesse, A. Mai, B. Tillack, and Y. Yamamoto, ECS Trans. **109**, 269 (2022).
28) Y. Yamamoto, W.-C. Wen, M. A. Schubert, A. A. Corley-Wiciak, S. Sugawa, Y. Ito, R. Yokogawa, A. Ogura, and B. Tillack, Extended Abstracts of the 2023 Int. Conf. on Solid State Devices and Materials, Nagoya, 2023, p. 527.
29) H. Tada, A. E. Kumpel, R. E. Lathrop, J. B. Slanina, P. Nieva, P. Zavracky, I. N. Miaoulis, and P. Y. Wong, J. Appl. Phys. **87**, 4189 (2000).
30) F. Pezzoli et al., Mater. Sci. Semicond. Proc. **11**, 279 (2008).
31) Y. Yamamoto, O. Skibitzki, M. A. Schubert, M. Scuderi, F. Reichmann, M. H. Zöllner, M. De Seta, G. Capellini, and B. Tillack, Jpn. J. Appl. Phys. **59**, SGGK10 (2020).
32) G. Rengo, C. Porret, A. Y. Hikavyy, E. Rosseel, N. Nakazaki, G. Pourtois, A. Vantomme, and R. Loo, ECS Trans. **98**, 27 (2020).
33) H. Jang, S. Koo, D.-S. Byeon, Y. Choi, and D.-H. Ko, J. Cryst. Growth **532**, 125429 (2020).